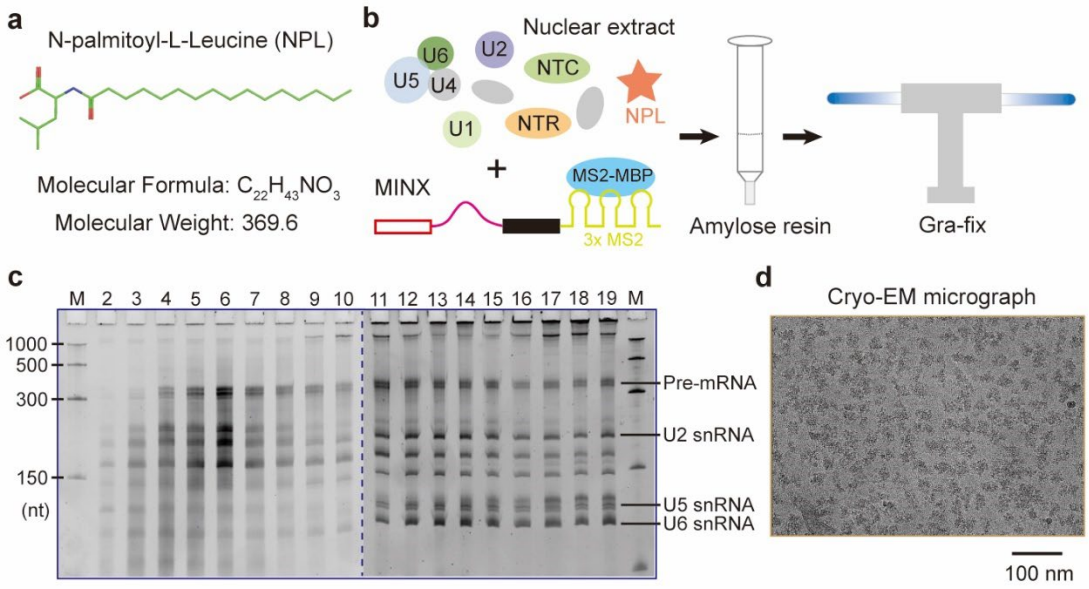

Supplementary Fig. 1 *In vitro* assembly and purification of human spliceosomal complexes.

a, The small molecule N-palmitoyl-L-Leucine (NPL). **b**, A schematic diagram of the protocol for *in vitro* assembly and isolation of human spliceosomal complexes. **c**, Analysis of the putative human spliceosomal complexes after glycerol gradient centrifugation with chemical crosslinking. Shown here are the results of urea PAGE gels. Source data are provided as a Source Data file. **d**, A representative cryo-EM micrograph of the human spliceosomal complexes. Scale bar, 100 nm.

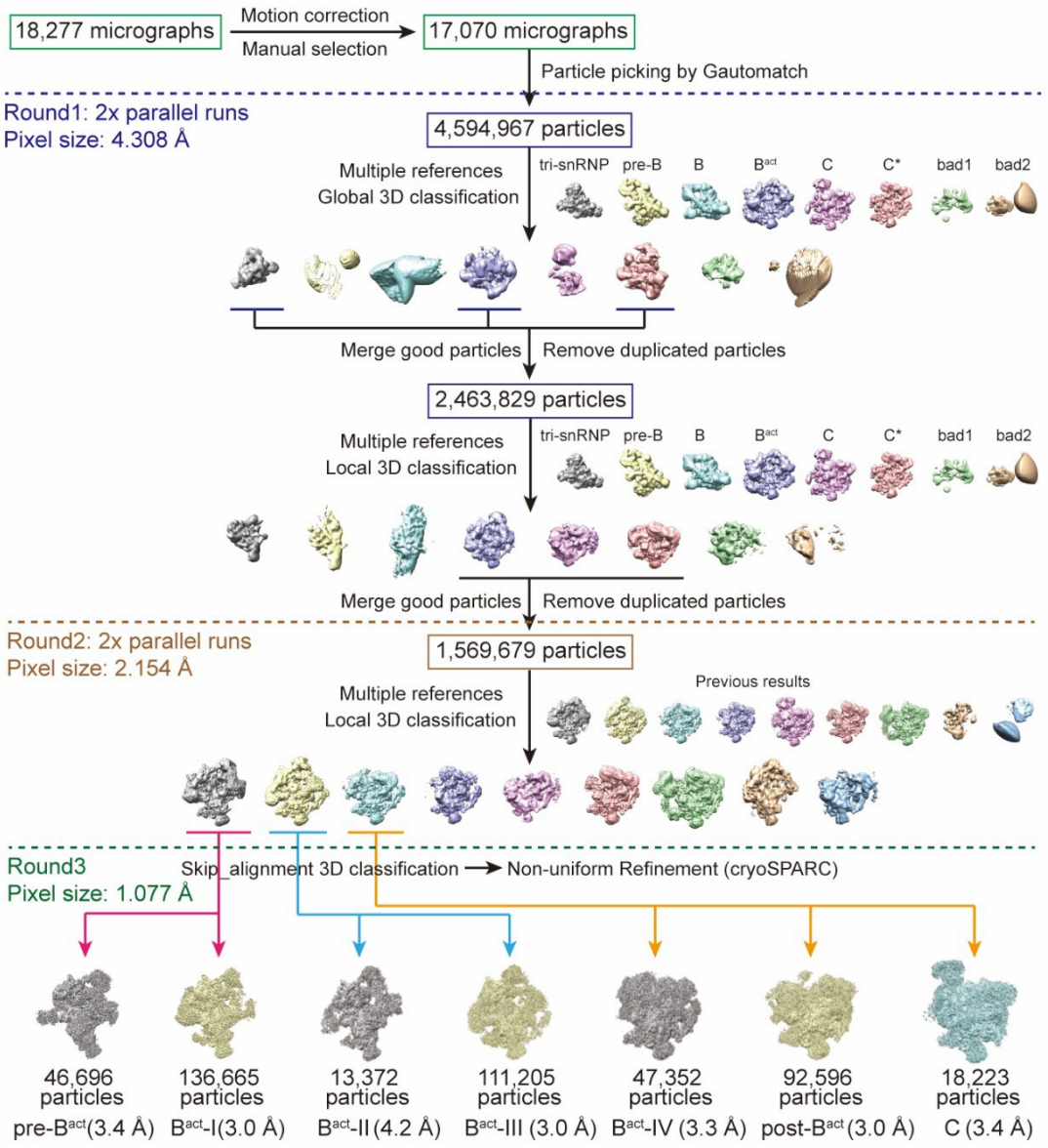

Supplementary Fig. 2 A flow chart of cryo-EM data processing for human activated spliceosomes and the C complex.

All processing steps were carried out in RELION 3.0 and cryoSPARC. Please refer to Methods for details.

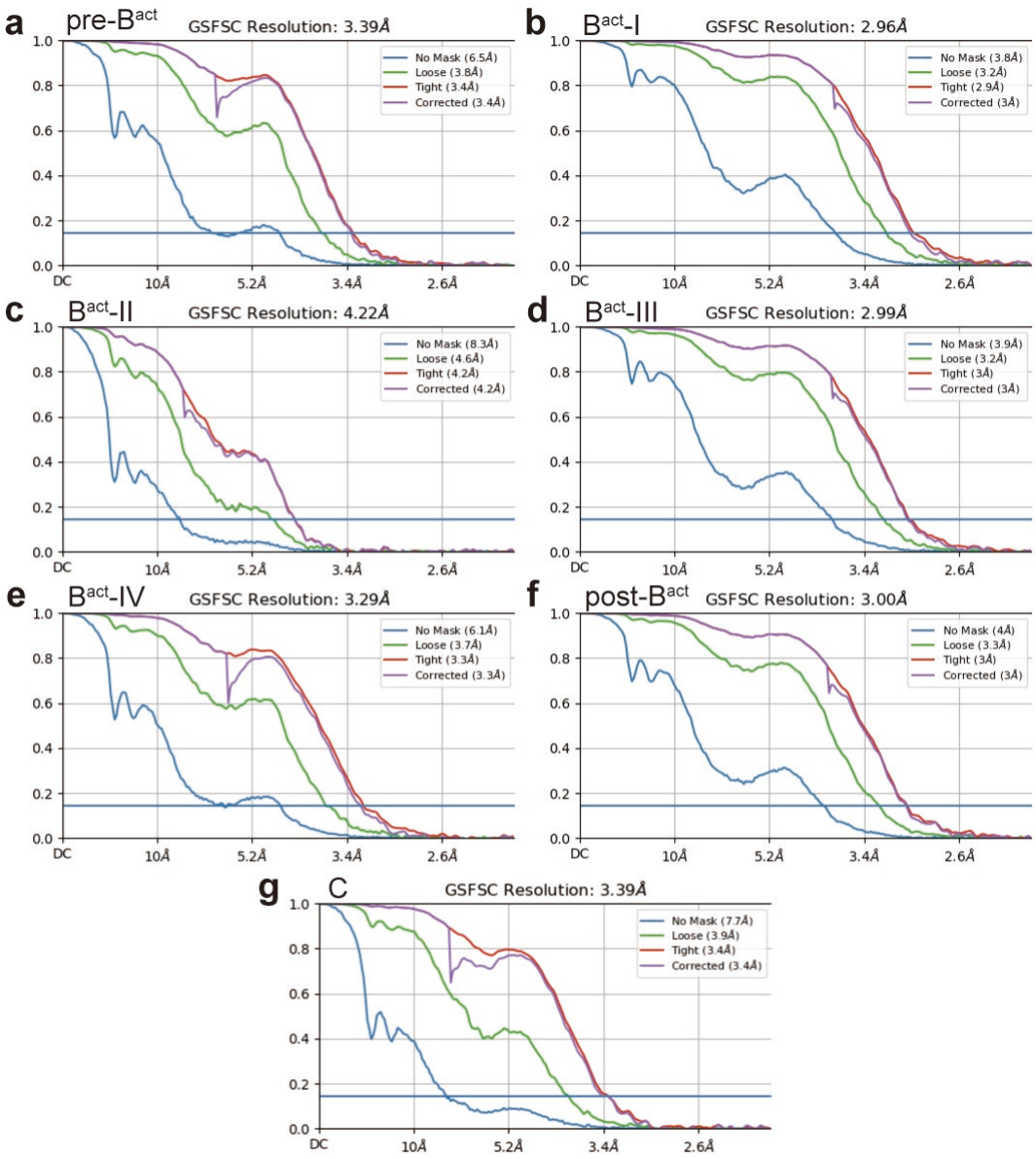

Supplementary Fig. 3 Cryo-EM reconstructions of the human activated spliceosomes and the C complex.

Shown here are the FSC curves for the final refinement in cryoSPARC. The average resolutions have been achieved at 3.4 Å for the human pre-B^{act} complex (**a**), 3.0 Å for the B^{act}-I complex (**b**), 4.2 Å for the B^{act}-II complex (**c**), 3.0 Å for the B^{act}-III complex (**d**), 3.3 Å for the B^{act}-IV complex (**e**), 3.0 Å for the post-B^{act} complex (**f**), and 3.4 Å for the C complex (**g**).

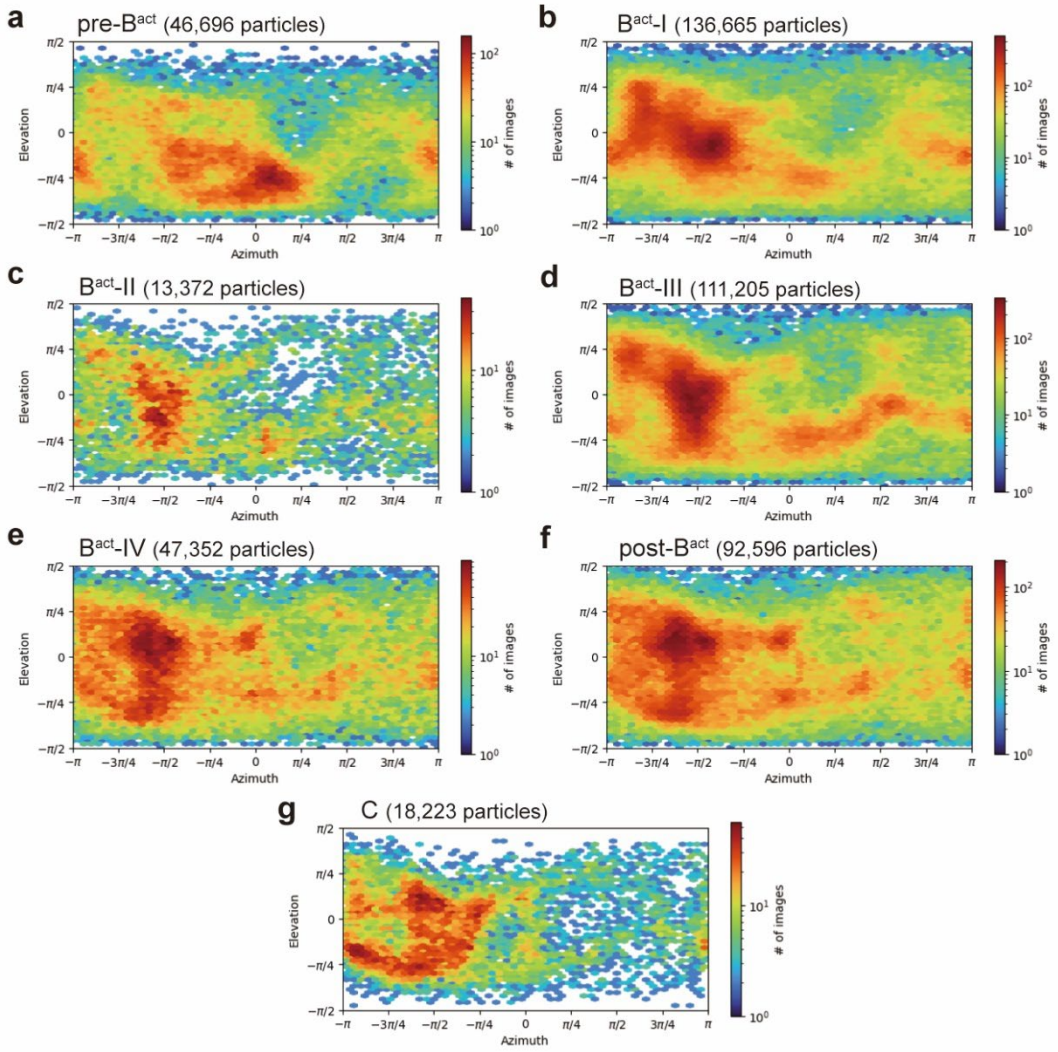

Supplementary Fig. 4 Angular distribution analysis of the human activated spliceosomes and the C complex.

Shown here are angular distribution of the particles used for the final reconstruction in cryoSPARC for the human pre-B^{act} complex (**a**), the B^{act}-I complex (**b**), the B^{act}-II complex (**c**), the B^{act}-III complex (**d**), the B^{act}-IV complex (**e**), the post-B^{act} complex (**f**), and the C complex (**g**).

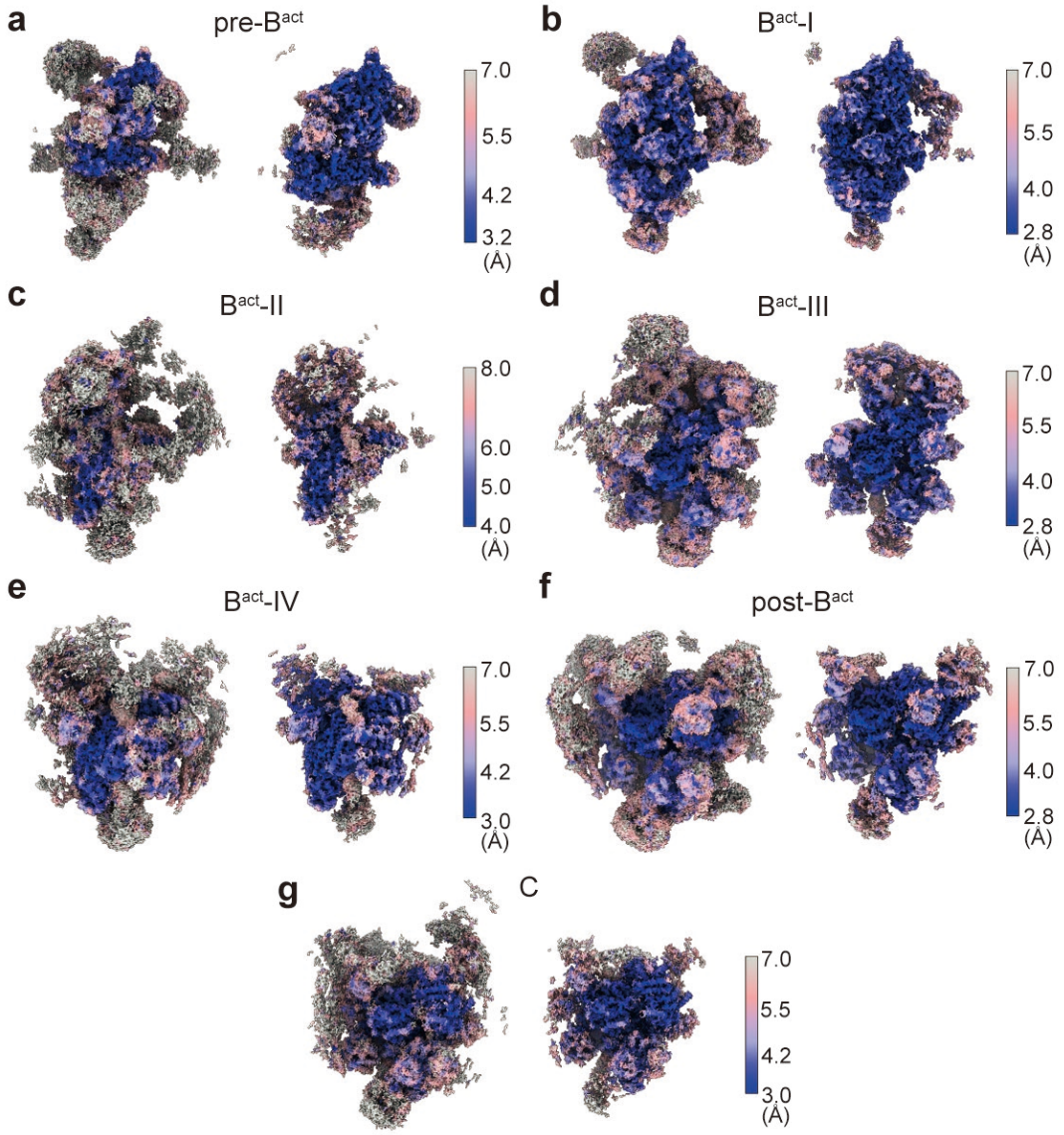

Supplementary Fig. 5 Overall EM maps of the human activated spliceosomes and the C complex.

Shown here in each panel are two views of the overall EM map with different count-levels for a distinct conformational state of the human spliceosome. The local resolutions are color-coded for different regions. The EM maps are shown for the human pre-B^{act} complex (**a**), the B^{act}-I complex (**b**), the B^{act}-II complex (**c**), the B^{act}-III complex (**d**), the B^{act}-IV complex (**e**), the post-B^{act} complex (**f**), and the C complex (**g**).

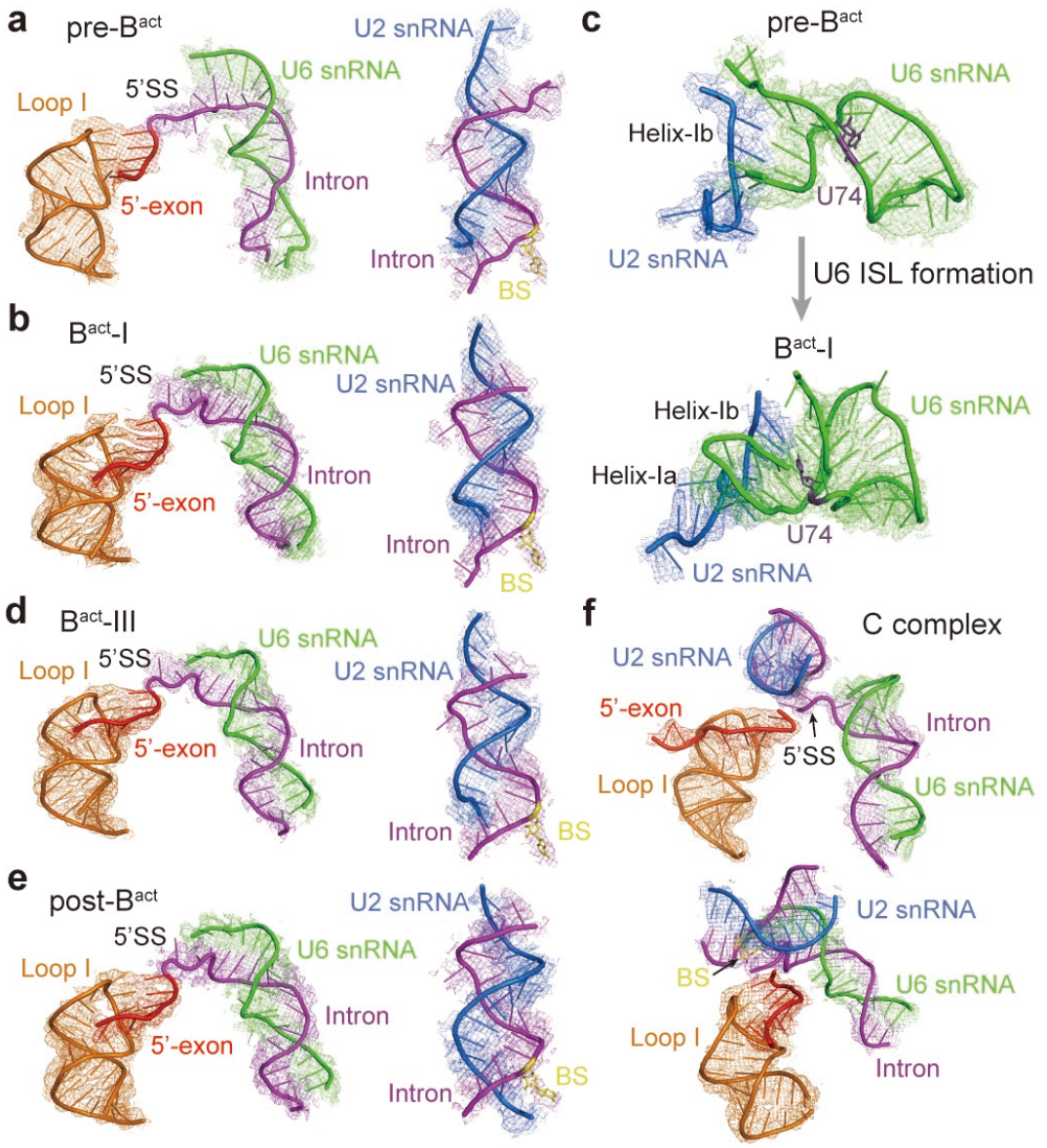

Supplementary Fig. 6 Representative EM maps of the RNA elements.
a, The EM maps of the 5'SS region (left panel) and the U2/BS duplex (right panel) in the pre-B^{act} complex. **b**, The EM maps of the 5'SS region (left panel) and the U2/BS duplex (right panel) in the B^{act}-I complex. **c**, The EM maps of the ISL of U6 snRNA in pre-B^{act} (upper panel) and B^{act}-I (lower panel). **d**, The EM maps of the 5'SS region (left panel) and the U2/BS duplex (right panel) in the B^{act}-III complex. **e**, The EM maps of the 5'SS region (left panel) and the U2/BS duplex (right panel) in the post-B^{act} complex. **f**, The EM maps of the RNA elements in the core region of the human C complex. Two independent views are shown. All EM density maps in this figure were prepared using PyMol with a contour level between 4σ and 9σ.

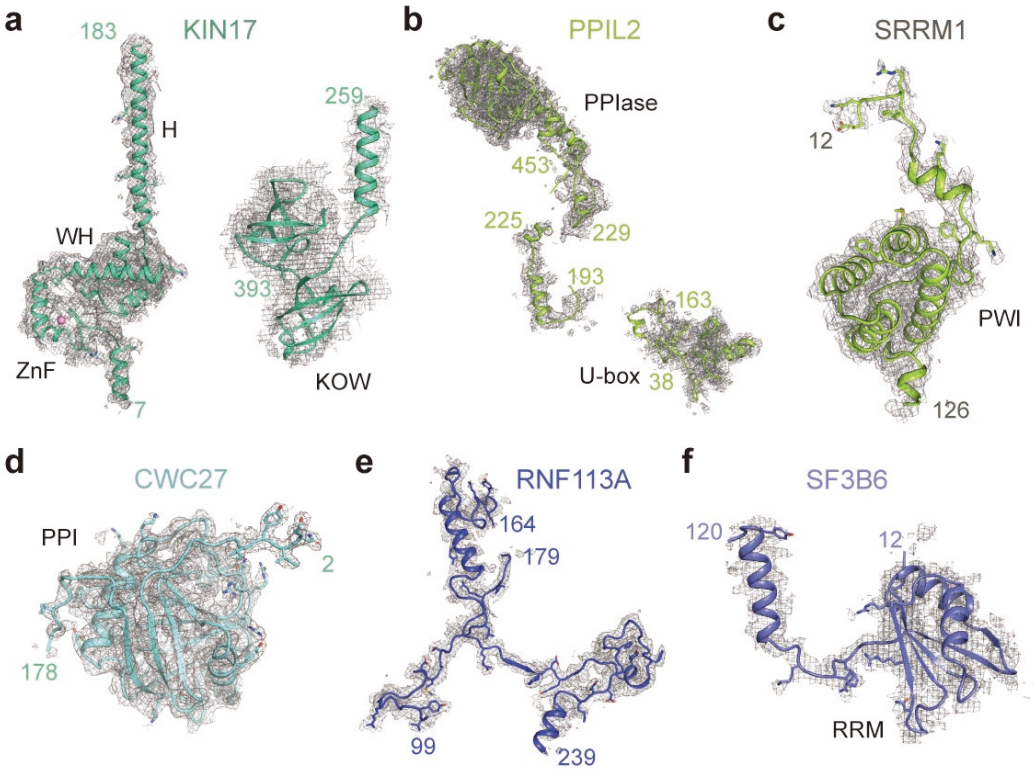

Supplementary Fig. 7 Representative EM maps of protein components in the pre-B^{act} and B^{act}-I complexes.

a, The EM maps of KIN17 in the pre-B^{act} complex. **b**, The EM maps of PPIL2 in the pre-B^{act} complex. **c**, The EM map of SRRM1 in the B^{act}-I complex. **d**, The EM map of CWC27 in the B^{act}-I complex. **e**, The EM map of RNF113A in the B^{act}-I complex. **f**, The EM map of SF3B6 in the B^{act}-I complex. All EM density maps in this figure were prepared using PyMol with a contour level between 3.5σ and 6σ.

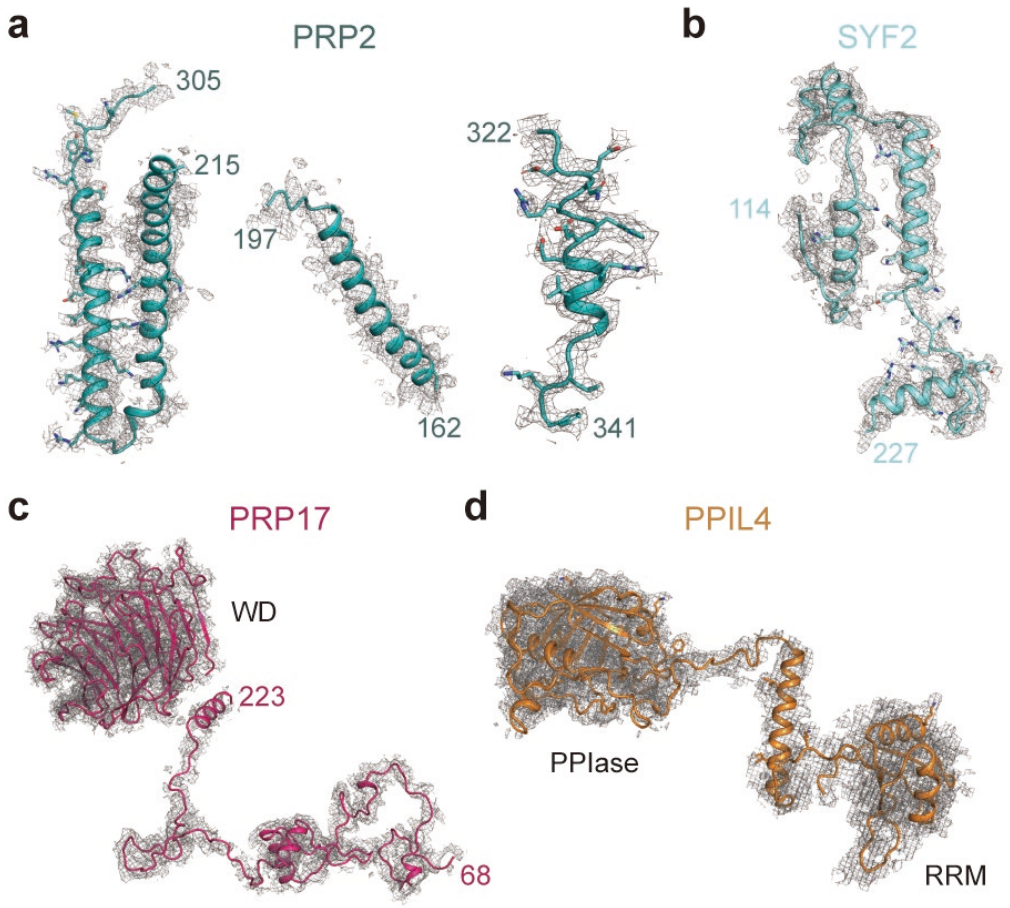

Supplementary Fig. 8 Representative EM maps of the protein components in the B^{act}-III and post-B^{act} complexes.

a, The EM maps for select secondary structural elements of the N-terminal extension from PRP2 in the B^{act}-III complex. **b**, The EM map of SYF2 in the post-B^{act} complex. **c**, The EM map of PRP17 in the post-B^{act} complex. **d**, The EM map of PPIL4 in the post-B^{act} complex. All EM density maps in this figure were prepared using PyMol with a contour level between 2σ and 5σ.

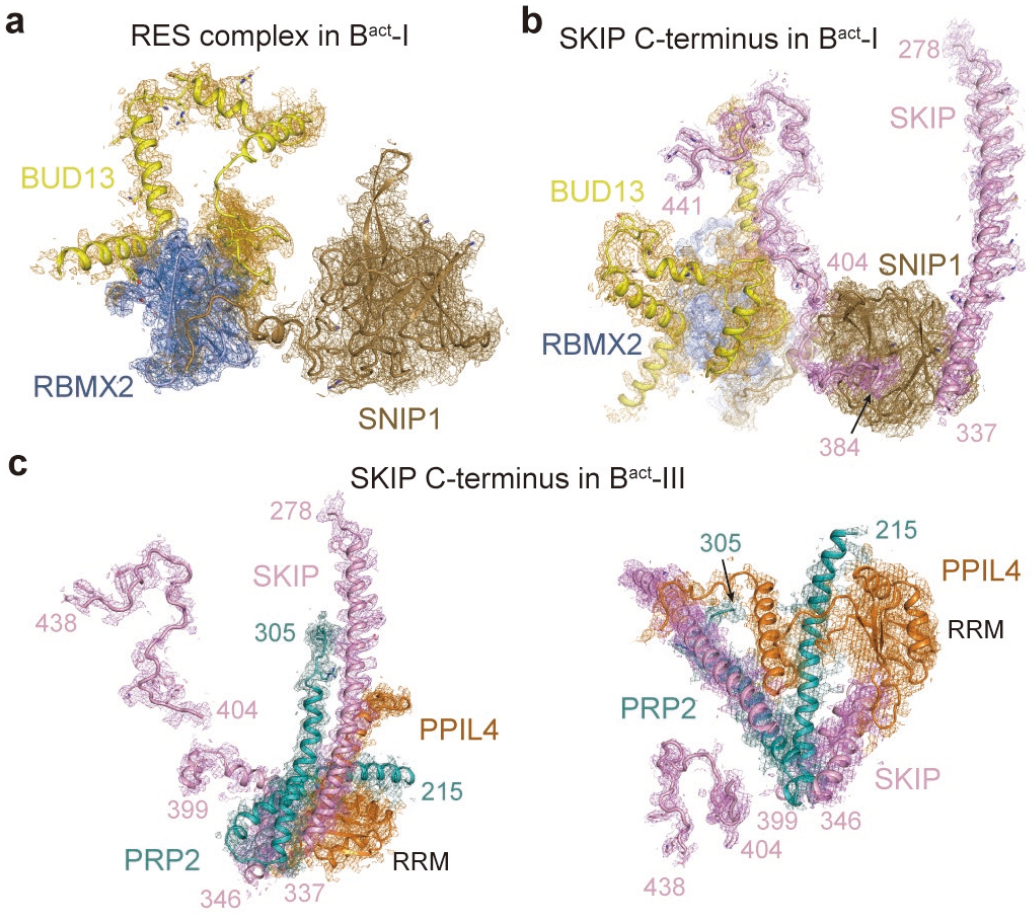

Supplementary Fig. 9 The EM maps of select protein interfaces.

a, The EM map of the RES complex in the B^{act}-I complex. **b**, The EM map of the interface between the C-terminus of SKIP and RES complex in B^{act}-I. **c**, The EM map of the interface among the C-terminal portions of SKIP, PPIL4, and PRP2 in the B^{act}-III complex. Two independent views are shown. All EM density maps in this figure were prepared using PyMol with a contour level between 4σ and 4.5σ.

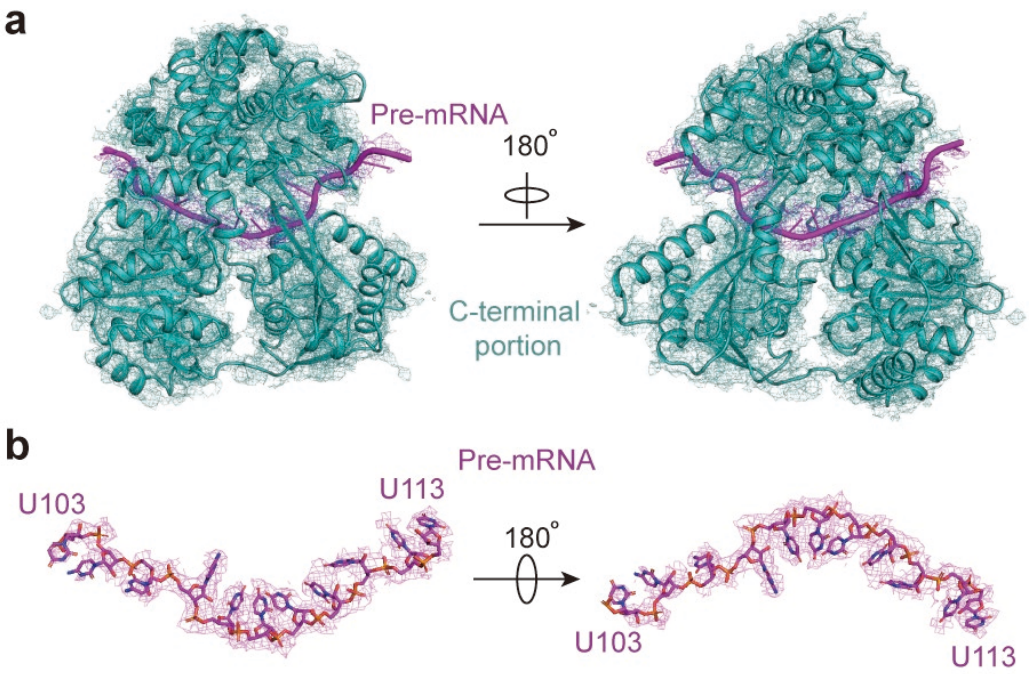

Supplementary Fig. 10 The EM maps for the C-terminal portion of PRP2 and the PPT sequences of pre-mRNA.

a, Two views of the EM maps for the C-terminal portion of PRP2 and the PPT sequences of pre-mRNA. **b**, The EM map of the PPT sequences of pre-mRNA. Two related views are shown. All EM density maps in this figure were prepared using PyMol with a contour level between 4σ and 4.5σ.

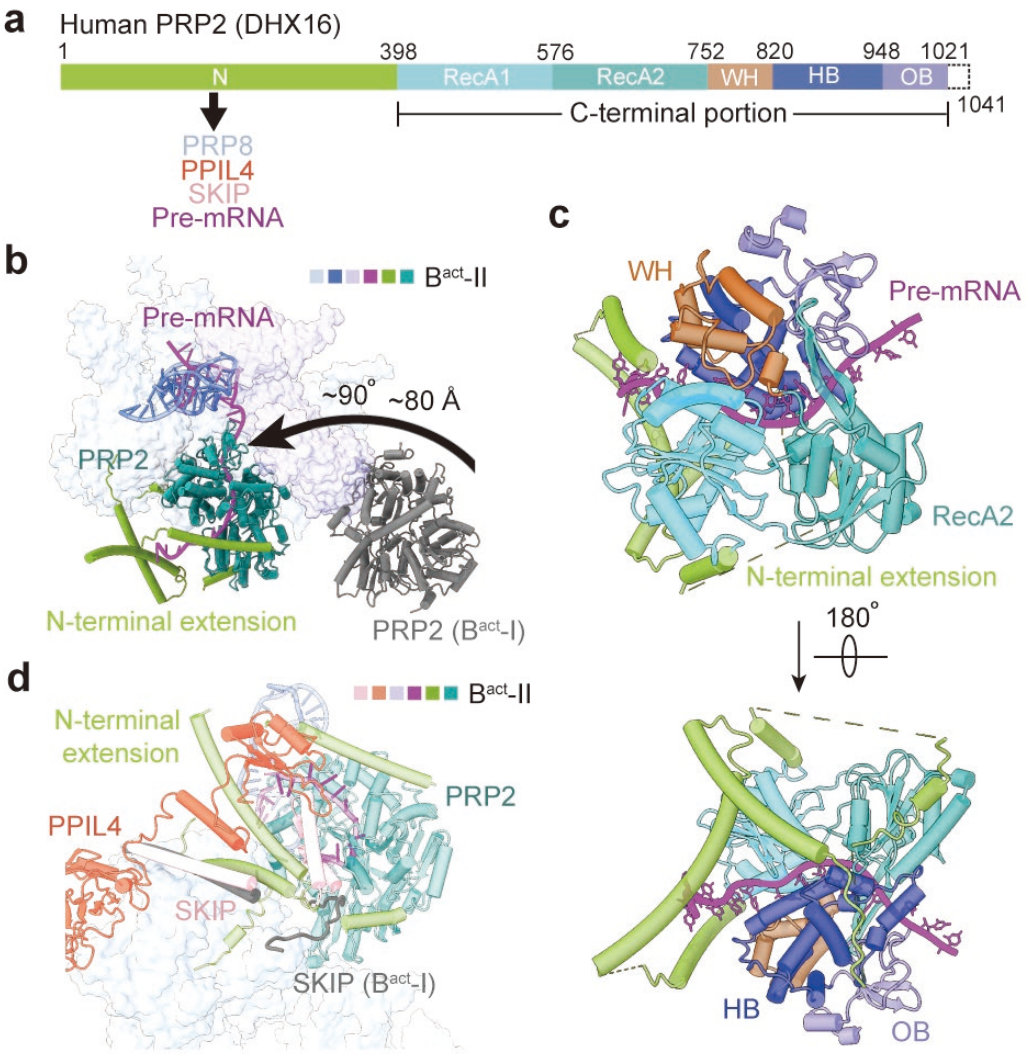

Supplementary Fig. 11 Structure features of PRP2.

a, Domain diagram of human PRP2. **b**, Positional shift of PRP2 in the transition of B^{act}-I to B^{act}-II. PRP2 is relocated over a distance of ~80 Å and a rotation of ~90 degrees to the cavity vacated by the RES complex. **c**, Structural features of PRP2 and the PPT sequences of pre-mRNA. **d**, The C-terminal portion of SKIP in the transition of B^{act}-I to B^{act}-II. The C-terminal flexible sequences of SKIP become ordered helices, contacting PRP2, PPIL4 and the 3'-end of PPT.

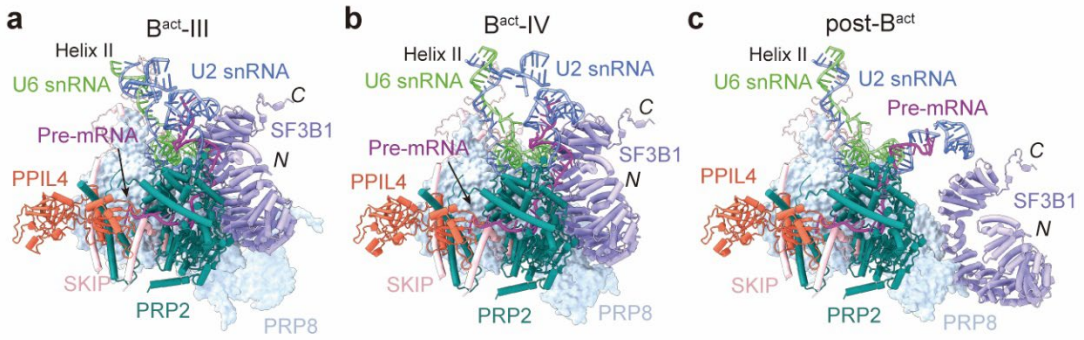

Supplementary Fig. 12 The structure of PRP2 in B^{act}-III, B^{act}-IV, and post-B^{act}. **a**, PRP2 in the B^{act}-III complex. **b**, PRP2 in the B^{act}-IV complex. The conformation of PRP2 in B^{act}-III or B^{act}-IV is almost identical to that in B^{act}-II. SF3B1 is translocated away from PRP8. Helix II and U2 snRNA also undergo large movements. **c**, PRP2 in the post-B^{act} complex. The conformation of PRP2 remains unchanged during the B^{act}-IV to post-B^{act} transition. But SF3B1 undergoes dramatic conformational changes, resulting in the release of the BS from its C-terminal HEAT repeats. U2 snRNA and the U2/BS duplex also experience notable conformational changes in the B^{act}-IV to post-B^{act} transition.

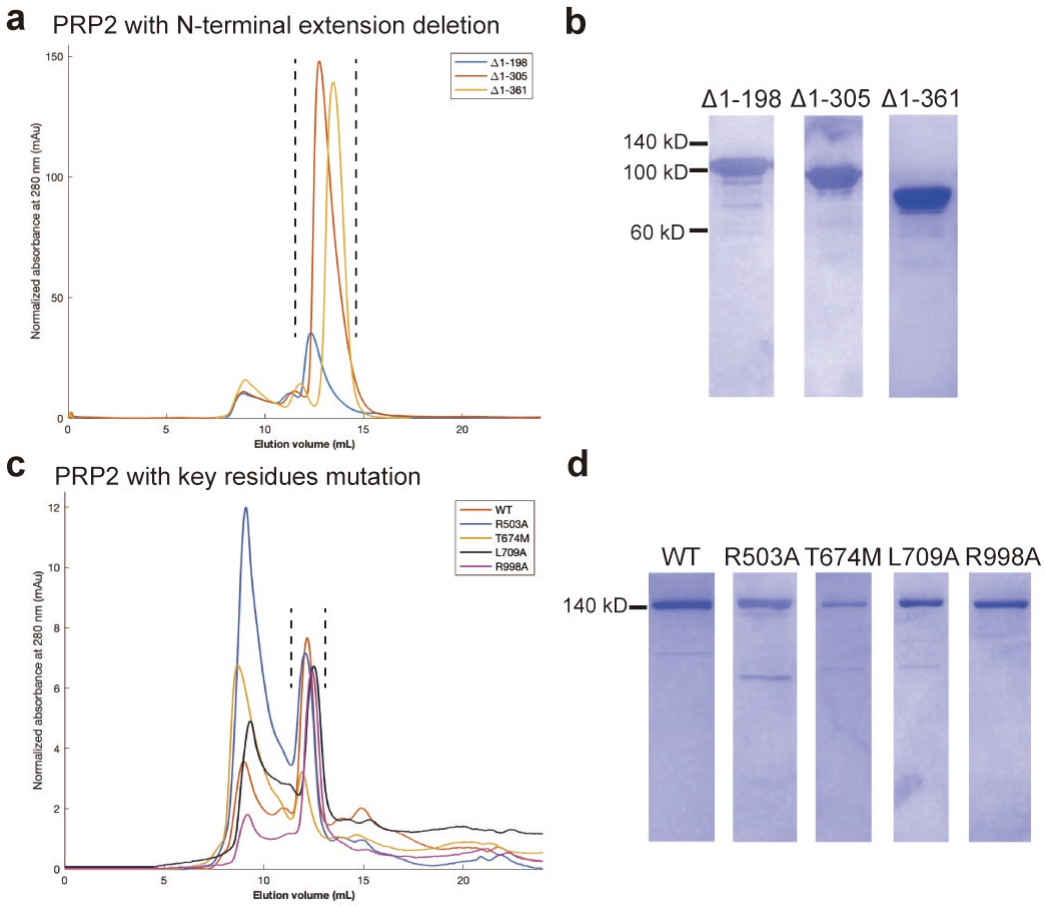

Supplementary Fig. 13 Purification of PRP2 and its variants.

a, Gel filtration chromatograms of three PRP2 N-terminal truncated variants. **b**, The gel filtration peak fractions of three PRP2 N-terminal truncated variants were visualized on SDS-PAGE. Source data are provided as a Source Data file. **c**, Gel filtration chromatograms of PRP2 missense variants. **d**, The gel filtration peak fractions of PRP2 missense variants were visualized on SDS-PAGE. Source data are provided as a Source Data file.

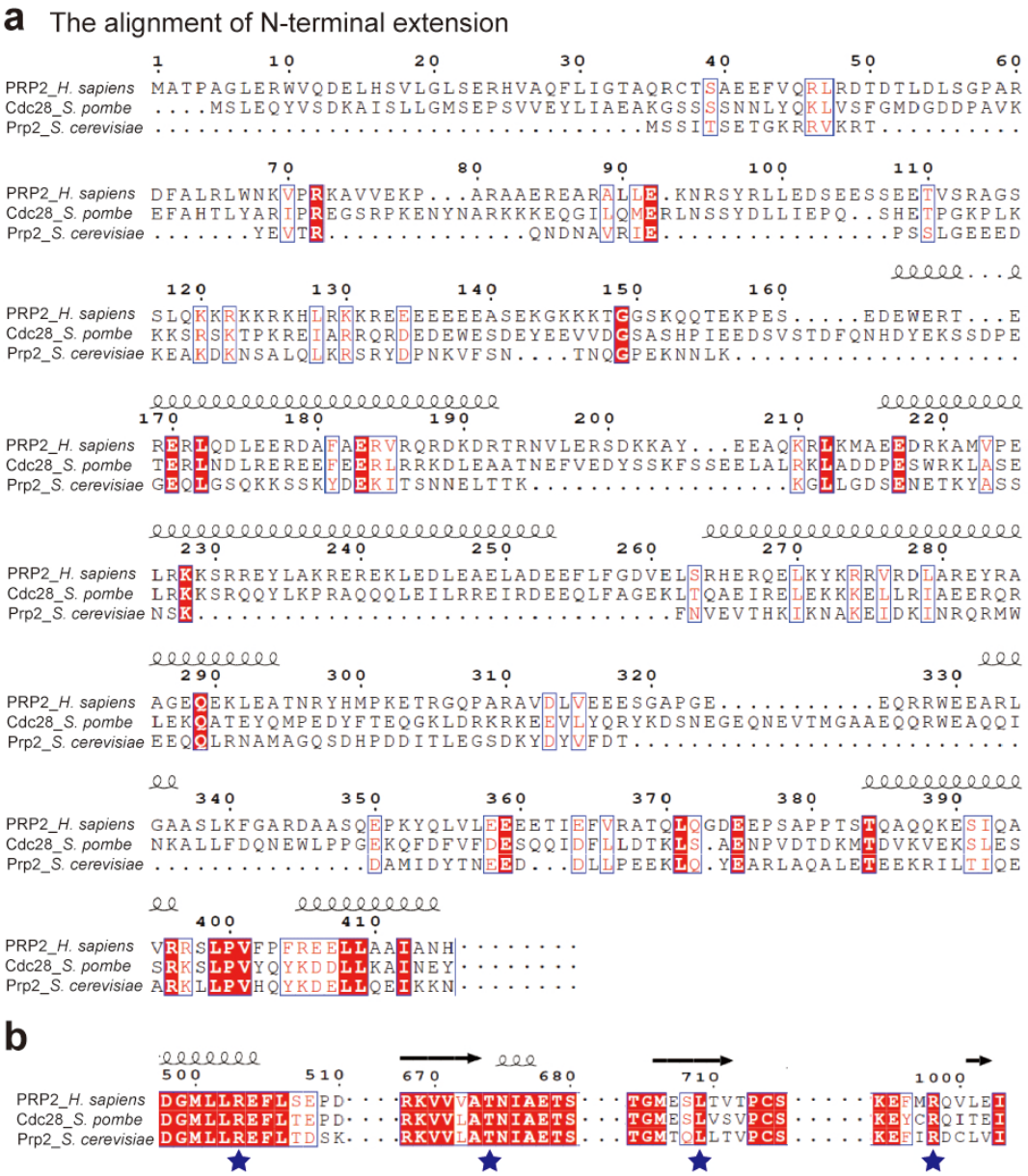

Supplementary Fig. 14 Sequence alignment of human PRP2 with its orthologs from *S. pombe* (Cdc28) and *S. cerevisiae* (Prp2) .

a, Sequence alignment among the N-terminal extensions of PRP2 and its orthologs. **b**, Sequence alignment among select sequence elements of PRP2 and its orthologs. Key residues of human PRP2 that contact the PPT of pre-mRNA are highly conserved and labeled with blue stars. Conserved amino acids are boxed. Invariant residues are highlighted in red background. The observed secondary structural elements are indicated above the sequences. The figure was generated using the ESPript server[1].

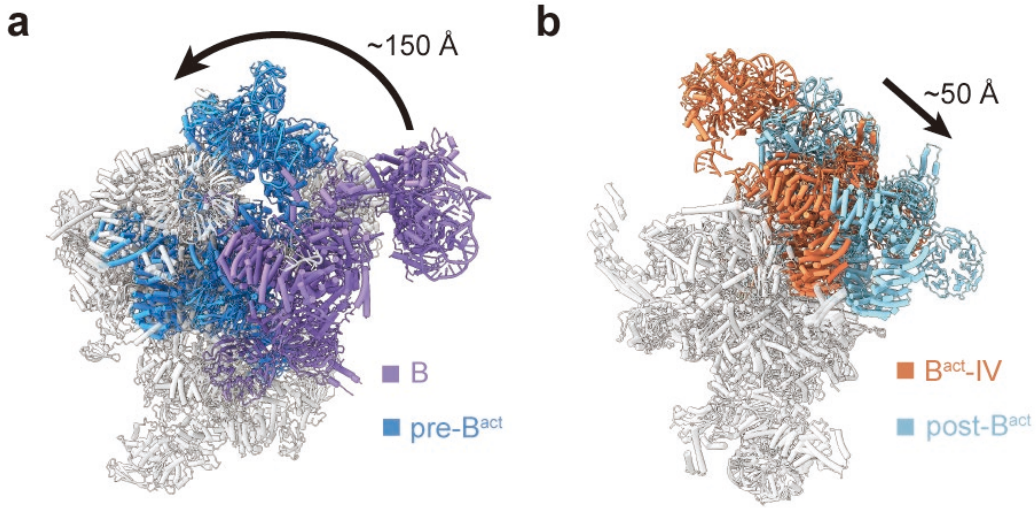

Supplementary Fig. 15 Structure rearrangements of U2 snRNP.
a, Structure rearrangements of U2 snRNP in the B to pre-B^{act} transition. U2 snRNP undergoes a remarkable translocation, moving over ~150 Å toward the main body of the spliceosome. **b**, Structure rearrangements of U2 snRNP in the B^{act}-IV to post-B^{act} transition. U2 snRNP travels ~50 Å, with its core moving closer to the main body of the spliceosome but the SF3b complex moving away from the main body.

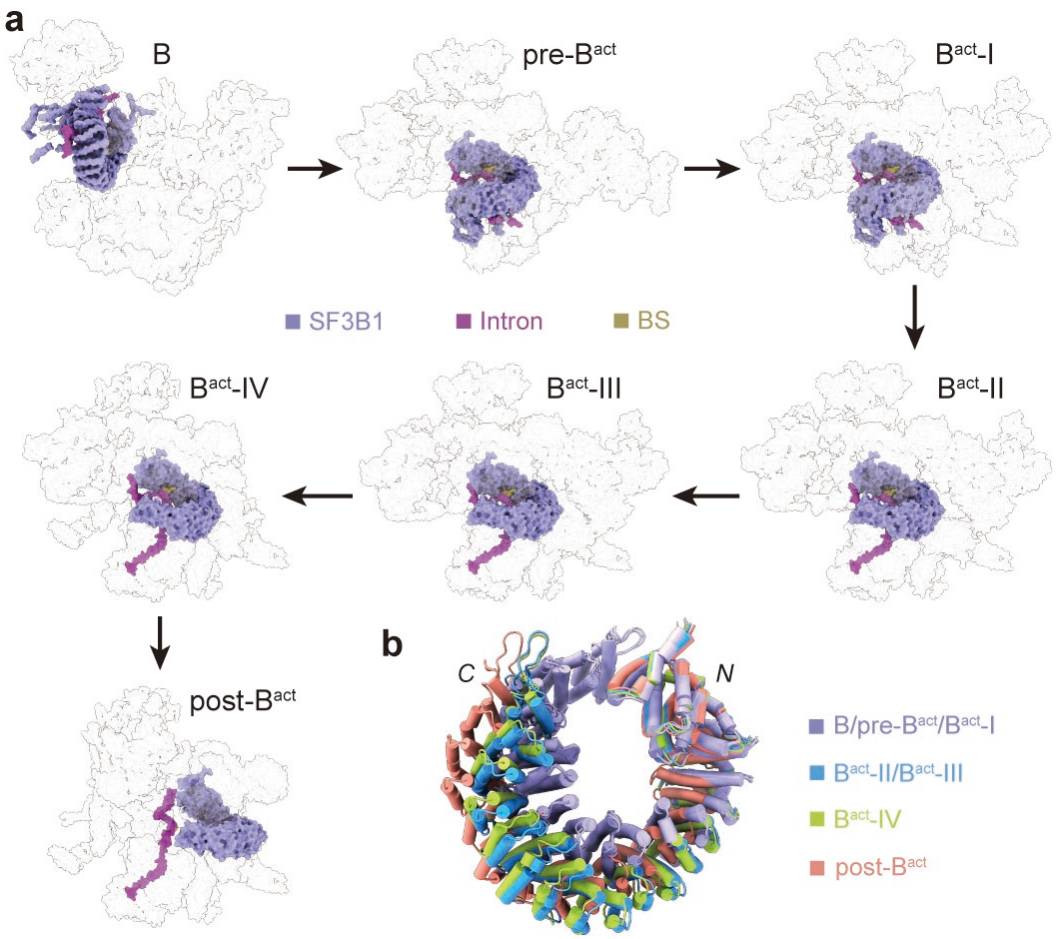

Supplementary Fig. 16 Conformational changes of SF3B1 during human spliceosome activation.

a, Conformational changes of SF3B1 and the intron sequences during spliceosome activation. The BS is freed from the C-terminus of SF3B1 in post-B^{act}, moving close to 5'SS. **b**, The local conformational changes of SF3B1. The superhelical SF3B1 becomes more extended and loosened during spliceosome activation.

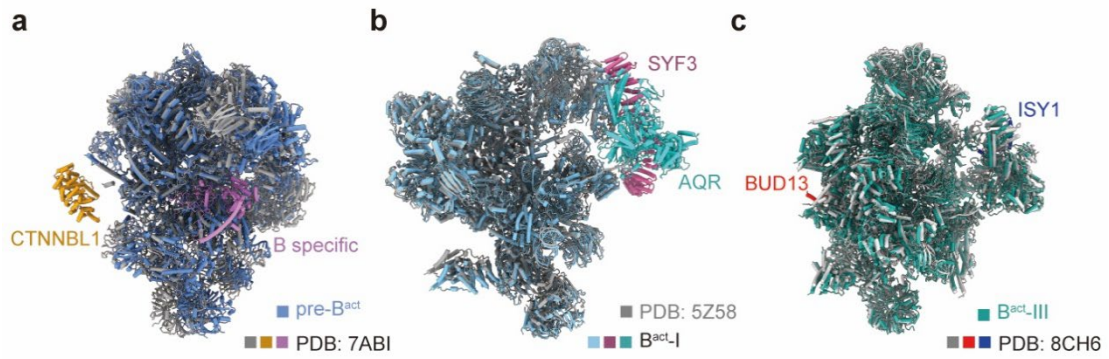

Supplementary Fig. 17 Structure comparison with previously reported B^{act} complexes.

a, Structure comparison of our pre-B^{act} complex with previously reported pre-B^{act-2} complex (PDB code: 7ABI)[2]. The B specific proteins (PRP38, SNU23, MFAP1 and UBL5) together with CTNNBL1 are absent in our pre-B^{act}, suggesting that pre-B^{act} may be downstream of pre-B^{act-2} in the splicing cycle. **b**, Structure comparison of B^{act}-I with previously reported early B^{act} complex (PDB code: 5Z58)[3]. **c**, Structure comparison of B^{act}-III with the reported B^{AQR} complex (PDB code: 8CH6)[4].

Supplementary Table 1 Statistics of 3D reconstructions and model refinement.

	Pre-B^{act}	B^{act}-I	B^{act}-II	B^{act}-III	B^{act}-IV	Post-B^{act}	C
Data collection							
EM equipment	FEI Titan Krios						
Voltage (kV)	300						
Detector	K3						
Magnification	81,000						
Pixel size (Å)	1.077						
Electron dose (e-/Å^2)	50						
Defocus range (μm)	-1.4 ~ -2.0						
Reconstruction							
Software	RELION 3.0/cryoSPARC						
Symmetry	C1						
Number of particles	46,696	136,665	13,372	111,205	47,352	92,596	18,223
Final masked resolution (Å)	3.4	3.0	4.2	3.0	3.3	3.0	3.4
Map sharpening B-factor (Å^2)	-62.3	-72.7	-59.9	-69.1	-61.0	-66.9	-47.9
EMDB code	EMD-35105	EMD-35107	EMD-35108	EMD-35109	EMD-35110	EMD-35111	EMD-35113
Model building							
Software	Coot-0.8.9/Chimera						
Refinement	Phenix						
Protein residues	15,020	16,510	16,147	17,516	15,091	14,853	15,844
RNA nucleotides	420	433	434	434	441	425	421
B factors (Å^2)	143.6	59.5	67.4	67.2	90.8	87.4	127.6
PDB code	8I0P	8I0R	8I0S	8I0T	8I0U	8I0V	8I0W
Validation							
R.m.s deviations							
Bonds length (Å)	0.011	0.011	0.012	0.011	0.011	0.011	0.012
Bonds Angle (°)	0.935	0.938	1.096	0.979	0.974	0.974	1.206
Ramachandran plot statistics (%)							
Preferred	90.74	91.46	89.09	88.81	91.04	92.21	93.75
Allowed	9.02	8.27	10.61	10.90	8.53	7.45	5.46
Outlier	0.24	0.27	0.30	0.29	0.44	0.35	0.79
Clashscore	22.92	15.01	26.54	21.23	22.59	16.23	18.16
CaBLAM outliers (%)	3.2	3.6	4.4	4.4	3.9	4.0	3.3
MolProbity score	3.25	3.10	3.44	3.36	3.24	3.28	2.53

Supplementary Table 2 Summary of modeled components in the human spliceosomal complexes.

Sub-complexes	Protein/RNA	Pre-B^{act}	B^{act}-I	B^{act}-II	B^{act}-III	B^{act}-IV	Post-B^{act}	C
U5 snRNP	U5 snRNA	√	√	√	√	√	√	√
	PRP8	√	√	√	√	√	√	√
	SNU114	√	√	√	√	√	√	√
	U5-40K	√	√	√	√	√	√	√
	SmB,D1,D2,D3,E,F,G	√	√	√	√	√	√	√
	BRR2	√	√	√	√			√
U6 snRNP	U6 snRNA	√	√	√	√	√	√	√
Pre-mRNA	Pre-mRNA	√	√	√	√	√	√	√
U2 snRNP	U2 snRNA	√	√	√	√	√	√	√
	U2-A'	√	√	√	√	√	√	√
	U2-B"	√	√	√	√	√	√	√
	SmB,D1,D2,D3,E,F,G	√	√	√	√	√	√	√
	SF3B1	√	√	√	√	√	√	
	SF3B2	√	√	√	√	√	√	
	SF3B3	√	√	√	√	√	√	
	SF3B4	√	√	√	√	√	√	
	SF3B5	√	√	√	√	√	√	
	SF3B6	√	√					
	PHF5A	√	√	√	√	√	√	
	SF3A1	√	√	√	√			
	SF3A2	√	√	√	√			
	SF3A3	√	√	√	√	√		
RES complex	SNIP1	√	√					
	RBMX2	√	√					
	BUD13	√	√					
PRP19/NTC complex	PRP19				√	√	√	√
	SPF27				√	√	√	√
	CDC5L	√	√	√	√	√	√	√
	CWC15	√	√	√	√	√	√	√
	PLRG1	√	√	√	√	√	√	√
NTC Related Complex	SYF2					√	√	√
	SYF3	√	√	√	√	√	√	√
	BUD31	√	√	√	√	√	√	√
	RBM22	√	√	√	√	√	√	√
	SNW1	√	√	√	√	√	√	√
	PPIL1			√	√	√	√	√
IBC	SYF1	√	√	√	√	√	√	√
	AQR	√	√	√	√	√	√	√
	PPIE	√	√	√	√	√	√	√

EJC	eIF4AIII							√
	MAGOH							√
	Y14							√
	MLN51							√
Splicing Factors	KIN17	√						
	SRRM1	√	√					
	PPIL2	√	√	√	√			
	CWC27		√					
	RNF113A		√	√	√	√		
	PRP2		√	√	√	√	√	
	SRRM2		√	√	√	√	√	√
	CWC22		√	√	√	√	√	√
	PPIL4			√	√	√	√	
	PRP17				√	√	√	√
	CCDC49							√
	CCDC94							√
	PRP16							√
	PPWD1							√
	WDR70							√
	FRG1							√
	CIR1							√

Under the column of each complex, colored boxes represent the presence of individual components in the complex.

References

1 Gouet, P., Courcelle, E., Stuart, D. I. & Metoz, F. ESPript: analysis of multiple sequence alignments in PostScript. *Bioinformatics* **15**, 305-308, doi:10.1093/bioinformatics/15.4.305 (1999).

2 Townsend, C. *et al.* Mechanism of protein-guided folding of the active site U2/U6 RNA during spliceosome activation. *Science* **370**, doi:10.1126/science.abc3753 (2020).

3 Zhang, X. *et al.* Structure of the human activated spliceosome in three conformational states. *Cell research*, doi:10.1038/cr.2018.14 (2018).

4 Schmitzova, J., Cretu, C., Dienemann, C., Urlaub, H. & Pena, V. Structural basis of catalytic activation in human splicing. *Nature* **617**, 842-850, doi:10.1038/s41586-023-06049-w (2023).